Journal of Power Sources 193 (2009) 871–877

Contents lists available at ScienceDirect

Journal of Power Sources

journal homepage: www.elsevier.com/locate/jpowsour

Structural analysis by synchrotron X-ray diffraction, X-ray absorption fine structure and transmission electron microscopy for aluminum-substituted α-type nickel hydroxide electrode

Masanori Morishita[a,*], Tadashi Kakeya[b], Seijiro Ochiai[b], Tetsuya Ozaki[b], Yoshiteru Kawabe[b], Masaharu Watada[b], Tetsuo Sakai[a,*]

[a] National Institute of Advanced Industrial Science and Technology, Kansai Center, 1-8-31 Midorigaoka, Ikeda, Osaka 563-8577, Japan
[b] GS Yuasa Corporation, Nishinosho, Kisshoin, Minami-Ku, Kyoto 601-8520, Japan

ARTICLE INFO

Article history:
Received 9 January 2009
Received in revised form 5 March 2009
Accepted 31 March 2009
Available online 8 April 2009

Keywords:
Nickel-metal hydride battery
Aluminum-substituted α-nickel hydroxide
Structural refinements

ABSTRACT

The detailed structural change in the charge–discharge process was investigated for the 20 mol% aluminum-substituted α-nickel hydroxide by using high-energy synchrotron X-ray diffraction (XRD), X-ray absorption fine structure (XAFS) and transmission electron microscopy (TEM) analysis. The 20 mol% aluminum-substituted α-nickel hydroxide showed the α-$Ni(OH)_2$/γ-NiOOH phase transformation in the charge–discharge process. The structural refinement has been done successfully on the basis of two phase models of the ideal phases and the fault ones, including the occupation sites for the potassium ions and H_2O (OH^-) molecules. The substituted aluminum ions were situated on both nickel sites and 18h sites in the interlayer. The α-$Ni(OH)_2$ structure would be stabilized by the presence of the aluminum ions on the 18h sites. The α-$Ni(OH)_2$ phases were transformed to the β-$Ni(OH)_2$ phases after 50 cycles because the aluminum ions on the 18h sites would be migrated from the bulk to the surface.

1. Introduction

Nickel-metal hydride (Ni-MH) battery has been widely used in the high power applications such as the power assist bicycles, the power tools and the hybrid electric vehicles (HEVs). Many studies have been done for the development of the high capacity Ni-MH battery. Spherical nickel hydroxide [$Ni(OH)_2$] was coated with the cobalt oxyhydroxide because of the increase of the active material utilization [1]. Rare earth–Mg–Ni-based alloys such as $La_{0.6}Pr_{0.2}Mg_{0.2}Ni_{3.2}Co_{0.3}(MnAl)_{0.2}$ showed the higher discharge capacity and the superior cycle performance as compared to the conventional alloy such as AB_5 and AB_2 phase [2].

Recently, α-$Ni(OH)_2$ has received much attention as active material for the positive electrode of advanced Ni-MH batteries. Larger discharge capacities could be obtained for α-$Ni(OH)_2$/γ-NiOOH redox couple because the oxidation state of nickel in the γ-NiOOH reaches 3.3–3.7 [3]. Pure α-$Ni(OH)_2$ is unstable in the alkaline electrolyte, being easily transformed to the β-$Ni(OH)_2$. The α-$Ni(OH)_2$ structure could be stabilized by the substitution of the nickel ions in the $Ni(OH)_2$ by the trivalent aluminum ions over 20 mol% [4–8]. The efforts were not successful because the aluminum ions were dissolved to the electrolyte in the charge–discharge process [7].

The ideal β-$Ni(OH)_2$ structure consists of close-packed oxygen planes with ABABAB stacking sequence along the *c* direction. Recently, two models of stacking faults have been reported to be exist in the β-$Ni(OH)_2$ structure, i.e., the growth fault and the deformation fault [9,10]. The both stacking faults lead to ABABCBCB and ABABCACA oxygen packing along the *c* direction, respectively. The presence of those stacking faults could explain the decrease in the X-ray diffraction (XRD) peak intensity.

The purpose of this work is to make clear the structural change in the charge–discharge process for the 20 mol% aluminum-substituted α-nickel hydroxide by using synchrotron XRD, X-ray absorption fine structure (XAFS) and transmission electron microscopy (TEM) analysis.

2. Experimental

The spherical aluminum-substituted α-nickel hydroxides (particle size: 10 μm) used in this work were prepared by the reaction crystallization process as follows: a mixed metal nitrate solution (1.6 mol dm^{-3} total concentration) containing the nickel and the aluminum in the required stoichiometric ratio ([Al]/[Ni + Al] = 20), 14 wt% of the ammonia solution and 40 wt% of the NaOH solution was added to the deionized water with constant stirring

* Corresponding authors. Tel.: +81 72 751 9611; fax: +81 72 751 9623.
E-mail addresses: m-morishita@aist.go.jp (M. Morishita), sakai-tetsuo@aist.go.jp (T. Sakai).

0378-7753/$ – see front matter © 2009 Elsevier B.V. All rights reserved.
doi:10.1016/j.jpowsour.2009.03.065

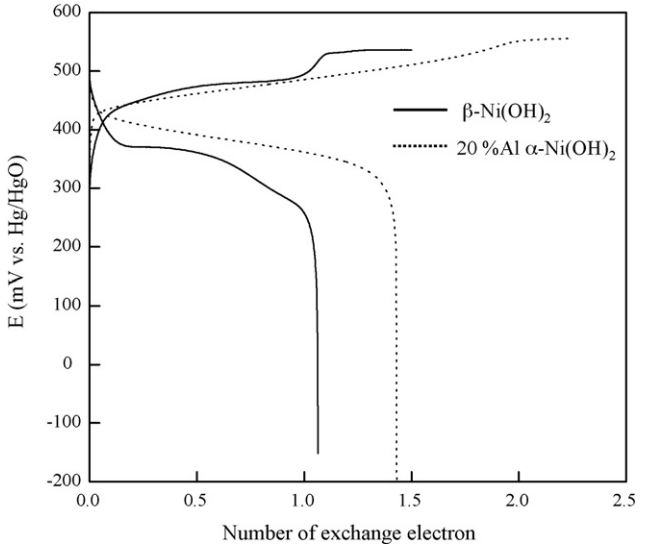

Fig. 1. The charge curves at the 0.15 C rate and the discharge curves at the 0.3 C rate for the Ni-MH test cells using β-Ni(OH)$_2$ and the 20% Al α-Ni(OH)$_2$.

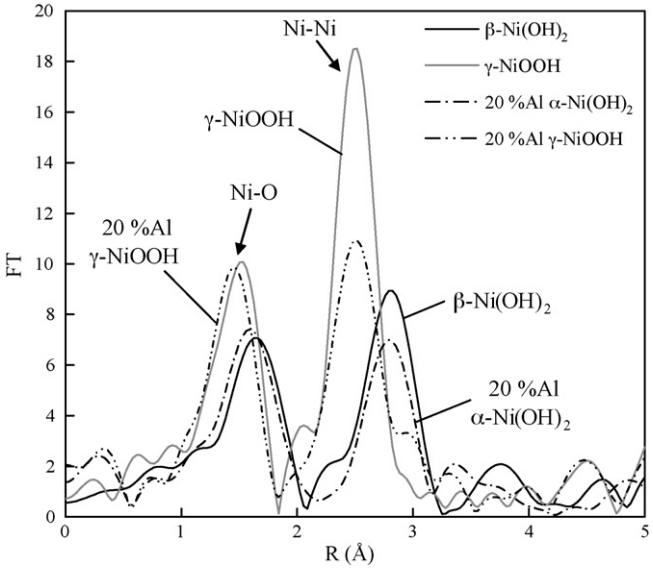

Fig. 3. Ni-K edge XAFS spectra for the 20% Al α-Ni(OH)$_2$ and the 20% Al γ-NiOOH.

at 45 °C. The pH of the solution was controlled in the range of 11–11.5. The precipitated green gel was filtered, washed copiously to neutralize, and then dried at 60–70 °C in air. The chemical compositions of the nickel and the aluminum in the aluminum-substituted nickel hydroxides were determined by an inductively coupled argon plasma emission spectrophotometer. The 20 mol% aluminum-substituted α-nickel hydroxide is called the 20% Al α-Ni(OH)$_2$.

The cobalt- and zinc-substituted β-nickel hydroxides used for the commercialized batteries were used as the standard materials for the comparison. The content of the cobalt and the zinc coprecipitated in the β-nickel hydroxide were 5.37 and 3.37 wt%, respectively. The β-nickel hydroxide is called the β-Ni(OH)$_2$.

The nickel hydroxide electrodes were prepared as follows: the nickel hydroxide powder was mixed with 10 wt% cobalt hydroxide powder, 0.5 wt% carboxymethyl cellulose and 0.5 wt% poly(tetrafluoroethylene) in order to make the slurry. The Co(OH)$_2$ was transformed to the CoOOH with high electrical conductivity in the charging process. This slurry was packed in a nickel foam substrate. After drying at 70 °C, the nickel hydroxide electrode was roll-pressed. The nickel hydroxide electrode was wrapped with a sulfonated-polypropylene nonwoven fabric separator, and then placed between two sheets of an MH electrode using an Mm(Ni, Co, Mn, Al)$_5$-type hydrogen storage alloy. These electrodes were sandwiched between two acryl resin plates, and then soaked into the 6.8 M KOH electrolyte. The Ni-MH test cell limited with the nickel hydroxide electrode capacity was constructed with the Hg/HgO electrode as a reference electrode.

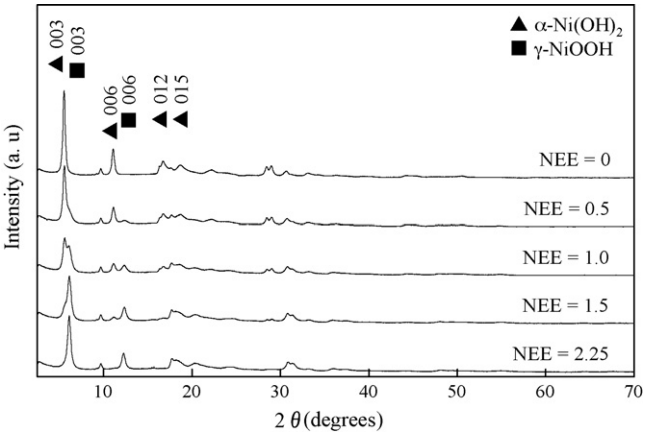

Fig. 2. The XRD patterns for the 20% Al α-Ni(OH)$_2$ obtained at various values of NEE.

The charge–discharge cycling test was carried out at 20 °C using a charge–discharge machine (2 V 10 A, Hokuto Denkou Ltd., Japan). For the activation, the nickel hydroxide electrode was charged at the 0.02 C rate for 12 h and 0.1 C rate for 9 h, and then discharged at the 0.3 C rate to 0 V vs. Hg/HgO electrode. The 20 and 50 charge–discharge cycles were performed by the charging at the 0.15 C rate and the discharging at the 0.3 C rate to 0 V vs. Hg/HgO electrode. The value of 1.0 for the number of exchanged electron (NEE) per one nickel atom corresponds to 100% of the depth of the charge (DOC). The nickel hydroxide electrodes were charged in the range of 50–225% of DOC, that is, 0.5–2.25 of NEE.

The nickel hydroxide electrodes were taken out from the test cells at the various values of NEE after 20 and 50 charge–discharge cycles, and then dried in the vacuum. The electrodes were cut in small pieces to get the nickel hydroxide powders. The metallic Ni due to the nickel foam was removed using the magnet from the powders.

The XRD measurement samples were prepared by filling the powders in the glass capillary of φ 0.3 mm. The XRD measurements were conducted using a large Debye–Scherrer camera with an imaging plate at the BL19B2 beam line, the synchrotron radiation facility

Table 1
The calibrated values of each shell for the pure β-Ni(OH)$_2$, the pure β-NiOOH, the pure γ-NiOOH, 20% Al α-Ni(OH)$_2$, and 20% Al γ-NiOOH.

Sample	Shell	Coordination number (N)	Distance (Å)	Debye–Waller factor (Å^2)
Pure β-Ni(OH)$_2$	Ni–O	6	2.074	0.069
	Ni–Ni	6	3.131	0.079
Pure β-NiOOH	Ni–O	6	1.916	0.076
	Ni–Ni	6	2.825	0.062
Pure γ-NiOOH	Ni–O	6	1.888	0.053
	Ni–Ni	6	2.840	0.060
20% Al α-Ni(OH)$_2$	Ni–O	6	2.047	0.080
	Ni–Ni	6	3.104	0.064
20% Al γ-NiOOH	Ni–O	6	1.880	0.056
	Ni–Ni	6	2.830	0.065

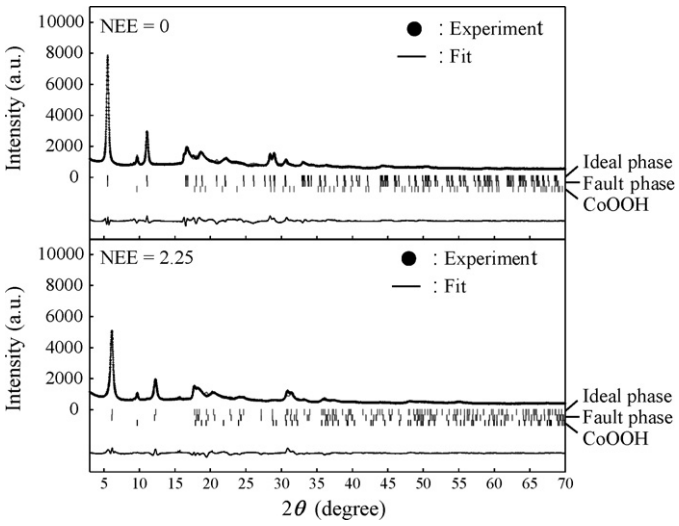

Fig. 4. The observed XRD patterns and calculated ones on the basis of the Rietveld refinements for the 20% Al α-Ni(OH)$_2$ obtained at NEE = 0 and 2.25.

SPring-8, Japan. The diffraction patterns were recorded in the 2θ range of 0.01–78°. The wavelength were calibrated to λ = 0.75 Å. The measurement time of the XRD was 300 s. The crystal structural analyses were conducted with the Rietveld method using the program RIETAN-2000 [11].

A β-Ni(OH)$_2$, a β-NiOOH synthesized electrochemically, and a γ-NiOOH synthesized chemically as follows were used as the standard materials for the X-ray absorption fine structure (XAFS) measurement. The β-NiOOH was prepared by charging the β-Ni(OH)$_2$ up to 1.5 times of the theoretical capacity (433 mAh g^{-1}) in the 7 M NaOH electrolyte, under which condition the γ-NiOOH was not formed. The γ-NiOOH was prepared by oxidizing chemically the β-Ni(OH)$_2$ in the 8 M KOH solution containing 12% sodium hypochlorite as an oxidizing reagent.

The nickel hydroxide powders were mixed with the boron nitride powders in order to make into pellets of 10 mm in diameter for the XAFS measurement. The XAFS measurement was conducted using the BL14B2 beam line at SPring-8, Japan. The measurement was conducted using the transmission detection modes at room temperature. The Ni K-edge XAFS spectra were recorded in the energy range of 8015–9855 eV. The measurement time of the XAFS spectra was 60 s. The exact values of each shell for the 20% Al α-Ni(OH)$_2$ were calibrated by using the program REX2000 [12].

The electron diffraction (ED) and the TEM analysis samples were prepared using a microtome machine. The ED patterns and the TEM images were taken with a JEOL JEM-3000F transmission electron microscopy at accelerating voltage of 300 kV. They were collected with the exposure for several seconds to minimize beam damage.

3. Results and discussion

Fig. 1 shows the charge–discharge curves of the Ni-MH test cells using the β-Ni(OH)$_2$ and the 20% Al α-Ni(OH)$_2$ after 20 charge–discharge cycles. The β-Ni(OH)$_2$ showed two plateaus corresponding to the β-Ni(OH)$_2$/β-NiOOH couple reaction and the oxygen evolution reaction in the charging process. The 20% Al α-Ni(OH)$_2$ showed a slowly increased charge potential, and the plateau potential for the oxygen evolution at the end of the charge. The NEE values are estimated to be 1.06 for the β-Ni(OH)$_2$, and 1.43 for the 20% Al α-Ni(OH)$_2$ in the discharging process. The discharge capacity for the 20% Al α-Ni(OH)$_2$ was higher than that for the β-Ni(OH)$_2$.

Fig. 2 shows the XRD patterns for the 20% Al α-Ni(OH)$_2$ obtained at various values of NEE. At NEE = 0, the XRD patterns could be identified as a pure α-Ni(OH)$_2$. With increasing the NEE values, the peak intensities due to the α-Ni(OH)$_2$ were decreased, while new peaks due to γ-NiOOH appeared at 7° and 12°. At NEE = 2.25, the XRD pattern were characterized as the γ-NiOOH. The 20% Al α-Ni(OH)$_2$ showed the α-Ni(OH)$_2$/γ-NiOOH phase transformation.

Fig. 3 shows the observed Ni-K edge XAFS spectra for the 20% Al α-Ni(OH)$_2$ and γ-NiOOH. The calibrated values of each shell for the samples using the program REX2000 are summarized in Table 1. The observed peaks at the shorter distance side would be ascribed to the first shell of the Ni–O bonds, and the ones at the longer distance side would be ascribed to the second shell of the Ni–Ni bonds. The calibrated values of the Ni–O and the Ni–Ni distance for the 20% Al α-Ni(OH)$_2$ were in good agreement with the expected values for the β-Ni(OH)$_2$. The nickel atom is surrounded by six oxygen atoms at a distance of about 2.04 Å. There are six nearest nickel atoms at a distance of about 3.10 Å. The calibrated values of the Ni–O and the Ni–Ni distances for the 20% Al γ-NiOOH were 1.88 and 2.83 Å, in good agreement with the expected values for the γ-NiOOH. Based on the XAFS results, the *z* positions of the oxygen were estimated to be 0.043 for the 20% Al α-Ni(OH)$_2$, and 0.041 for the 20% Al γ-NiOOH, respectively. Those values were used for the Rietveld refinements.

Table 2
Summary of the *R* factors and the crystallographic parameters for the 20 mol% Al α-Ni(OH)$_2$ and γ-NiOOH obtained at various values of NEE determined by the Rietveld refinements.

NEE	Phase	R_{wt} (%)	*Re* (%)	*S*	Cell parameters (Å)	Volume (Å^3)	Content (wt%)
0	Ideal α-Ni(OH)$_2$	5.53	3.44	1.6053	*a* = 3.079 (1), *c* = 23.70 (4)	194.6	75.5
	Fault α-Ni(OH)$_2$				*a* = 3.077 (6), *c* = 23.71 (5)	194.5	20.1
0.5	Ideal α-Ni(OH)$_2$	4.45	3.56	1.2482	*a* = 3.075 (2), *c* = 23.69 (4)	194.0	56.3
	Fault α-Ni(OH)$_2$				*a* = 3.078 (6), *c* = 23.71 (5)	194.5	12.8
	Ideal γ-NiOOH				*a* = 2.868 (3), *c* = 21.37 (2)	152.3	17.3
	Fault γ-NiOOH				*a* = 2.865 (3), *c* = 21.41 (2)	152.3	9.9
1.0	Ideal α-Ni(OH)$_2$	4.05	3.70	1.0934	*a* = 3.077 (2), *c* = 23.69 (5)	194.3	40.2
	Fault α-Ni(OH)$_2$				*a* = 3.079 (1), *c* = 23.71 (8)	194.6	8.12
	Ideal γ-NiOOH				*a* = 2.863 (2), *c* = 21.37 (7)	151.7	36.8
	Fault γ-NiOOH				*a* = 2.865 (8), *c* = 21.44 (8)	152.5	12.4
1.5	Ideal α-Ni(OH)$_2$	4.69	3.74	1.2546	*a* = 3.075 (2), *c* = 23.67 (1)	193.8	16.9
	Fault α-Ni(OH)$_2$				*a* = 3.078 (3), *c* = 23.69 (1)	194.4	1.2
	Ideal γ-NiOOH				*a* = 2.868 (1), *c* = 21.39 (4)	152.4	60.6
	Fault γ-NiOOH				*a* = 2.871 (6), *c* = 21.43 (7)	152.9	18.6
2.25	Ideal γ-NiOOH	5.73	3.92	1.4624	*a* = 2.863 (1), *c* = 21.39 (4)	151.9	78.8
	Fault γ-NiOOH				*a* = 2.871 (7), *c* = 21.43 (5)	153.0	19.1

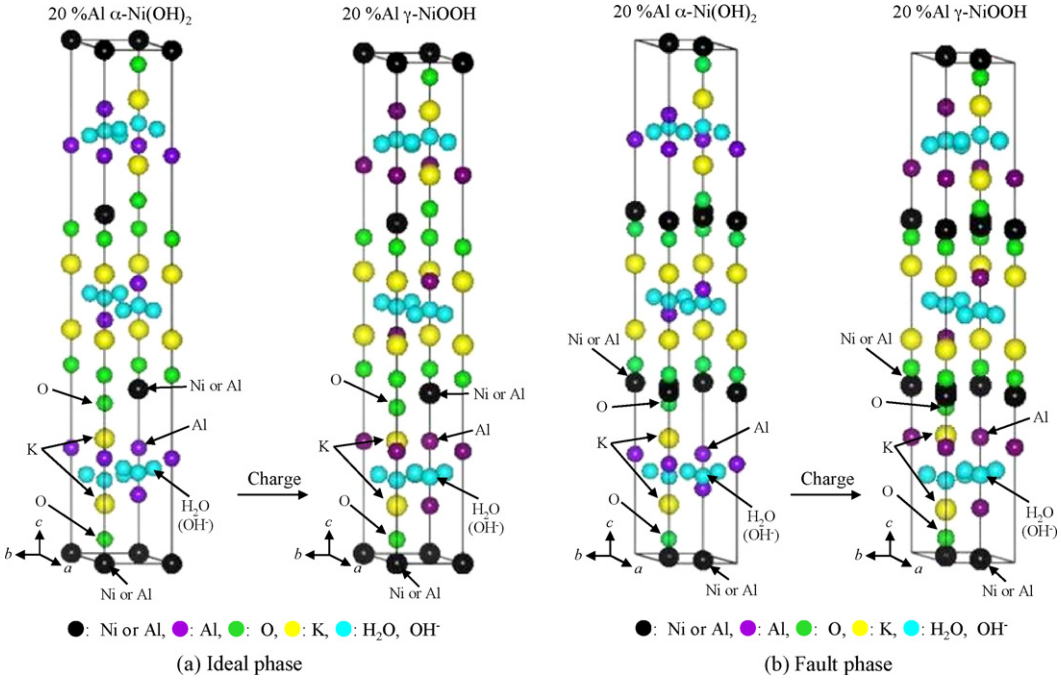

Fig. 5. Structural models of the ideal phases and the fault phases for the 20% Al α-Ni(OH)$_2$ and 20% Al γ-NiOOH.

Fig. 4 compares the observed XRD patterns and calculated ones on the basis of the Rietveld refinements for the 20% Al α-Ni(OH)$_2$ at various values of NEE after 20 charge–discharge cycles. When the previous structural models constituted with only the nickel ions and the oxygen ions were applied to the 20% Al α-Ni(OH)$_2$ [13,14], it was difficult to refine those structures due to the low degree of the crystallinity of the nickel hydroxides and the broadening of the XRD peaks.

We have succeeded in refining the structural data of synchrotron XRD and XAFS obtained for the 20% Al α-Ni(OH)$_2$ on the basis of the following assumptions. (i) The fault phases such as the staking fault exist in the 20% Al α-Ni(OH)$_2$. The nickel ions occupy the (0, 0, 0) sites for the ideal phases and the (2/3, 1/3, 0) sites for the fault ones, causing the decrease in the peak intensities; (ii) the substituted aluminum ions could occupy both nickel sites and 18h sites in the interlayer; (iii) the intercalated potassium ions and H_2O molecules are located on the 6c and 18h sites, respectively. As shown in Fig. 4, the R_{wp} values of those patterns were below 10%, showing good agreement between the observed and calculated patterns. The structural parameters for the 20% Al α-Ni(OH)$_2$ at various values of NEE derived from the Rietveld refinements are summarized in Table 2.

The structural models of the ideal and fault phases for a 20% Al α-Ni(OH)$_2$ (a) and a 20% Al γ-NiOOH (b) is illustrated in Fig. 5. The α-Ni(OH)$_2$ was refined with the *R*-3*m* space group, which has the highest symmetry among rhombohedral systems. This structure consists of the oxygen planes with an AABBCC stacking sequence. The nickel ions occupied the (0, 0, 0) sites for the ideal α-Ni(OH)$_2$ phases and the (2/3, 1/3, 0) sites for the fault ones, respectively. The aluminum ions were situated on both the nickel sites and the 18h sites in the interlayer because the aluminum ions could not be situated on the nickel sites over 10 mol%. The α-Ni(OH)$_2$ structure could be stabilized by the presence of the aluminum ions on the 18h sites.

The γ-NiOOH was built with the *R*-3*m* symmetry rule. The nickel ions occupied the (0, 0, 0) sites for the ideal γ-NiOOH phases and the (2/3, 1/3, 0) sites for the fault ones, respectively. The *z* positions of the oxygen ions were changed from 0.043 to 0.041 by the

Table 3
The atomic parameters for the 20% Al α-Ni(OH)$_2$ and γ-NiOOH used for the Rietveld refinements. *g* = Site occupancy, *B* = overall isotropic atomic displacement parameter.

	Ideal α-Ni(OH)$_2$ (space group: $R\bar{3}m$)					Fault α-Ni(OH)$_2$ (space group: $R\bar{3}m$)				
	x	*y*	*z*	*g*	*B* (Å^2)	*x*	*y*	*z*	*g*	*B* (Å^2)
M (3a1)	0	0	0	1	0.5	2/3	1/3	0	1	0.5
Al (18hl)	0.6666	−*x*	0.5387	0.0167	0.6485	0.6668	−*x*	0.5271	0.0167	0.2729
O1 (6c1)	1/3	−1/3	0.0430	1	0.5	1/3	−1/3	0.0430	1	0.5
K (6c2)	1/3	−1/3	0.1031	0.1655	0.5603	1/3	−1/3	0.1024	0.2268	0.3667
O2 (18h2)	0.184	−*x*	0.5103	0.1270	0.6843	0.184	−*x*	0.5031	0.4270	0.3873
	(M; Ni:Al = 9:1, O_2; OH^- or H_2O)									
	Ideal γ-NiOOH (space group: $R\bar{3}m$)					Fault γ-NiOOH (space group: $R\bar{3}m$)				
	x	*y*	*z*	*g*	*B* (Å^2)	*x*	*y*	*z*	*g*	*B* (Å^2)
M (3al)	0	0	0	1	0.5	2/3	1/3	0	1	0.5
Al (18hl)	0.6669	−*x*	0.5576	0.0167	0.0299	0.6668	−*x*	0.5641	0.0167	0.7645
O1 (6c1)	1/3	−1/3	0.0410	1	0.5	1/3	−1/3	0.0410	1	0.5
K (6c2)	1/3	−1/3	0.1028	0.2877	0.1532	1/3	−1/3	0.0929	0.3673	0.3807
O2 (18h2)	0.184	−*x*	0.5055	0.1557	1.0570	0.184	−*x*	0.4859	0.4559	0.3267
	(M; Ni:Al = 9:1, O_2; OH or H_2O)									

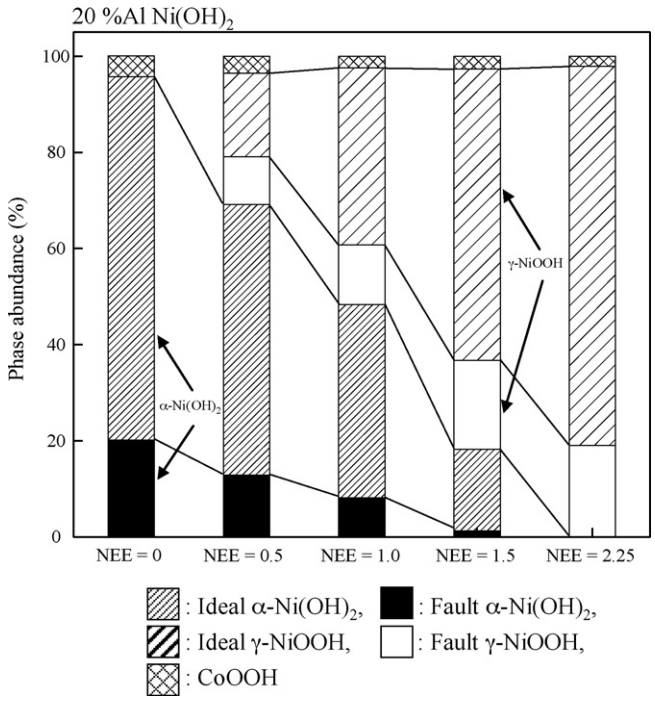

Fig. 6. The phase abundance for the 20% Al α-Ni(OH)$_2$ obtained at various values of NEE.

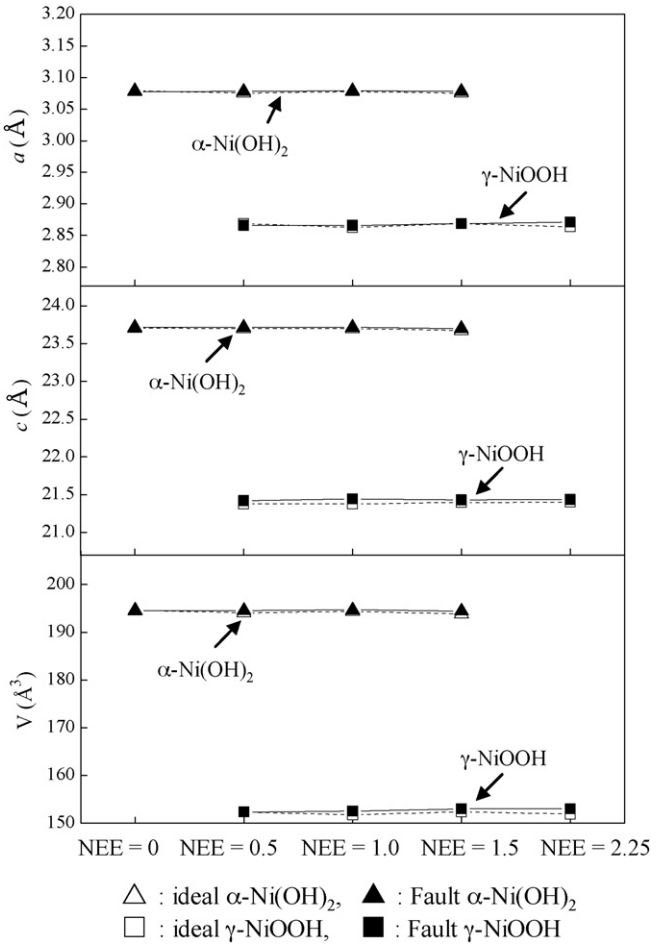

Fig. 7. The lattice parameters for the 20% Al α-Ni(OH)$_2$ and 20% Al γ-NiOOH obtained at various values of NEE.

phase transformation from the α-Ni(OH)$_2$ to the γ-NiOOH because of the decrease in the ionic radius of the nickel ions. On the charging process, the aluminum ions on the nickel sites did not migrate, while those on 18h sites slightly migrated. The intercalated potassium ions and H_2O (OH^-) molecules were located on 6c and 18h sites in both the α-Ni(OH)$_2$ and γ-NiOOH phases, respectively. It was found that the fault α-Ni(OH)$_2$ and γ-NiOOH phases contained a larger amount of the potassium ions and H_2O (OH^-) molecules than the ideal ones. The atomic parameters for the 20% Al α-Ni(OH)$_2$ and γ-NiOOH used for the Rietveld refinements are summarized in Table 3.

Fig. 6 shows phase abundance for the 20% Al α-Ni(OH)$_2$ obtained at various values of NEE. At NEE = 0, the phase abundance for the ideal and fault α-Ni(OH)$_2$ phases was 76 and 20%, respectively. The phase abundance for the γ-NiOOH phases was increased with the increase in the NEE values. The total amount of the γ-NiOOH phases reached 27% at NEE = 0.5, 49% at NEE = 1.0, and 79% at NEE = 1.5. At NEE = 2.25, the α-Ni(OH)$_2$ phases were completely transformed to the γ-NiOOH phases. The phase abundance for the ideal and fault γ-NiOOH phases was 79 and 19%, respectively. The CoOOH as conductive materials appeared at all the NEE values.

Fig. 7 shows the change of the lattice parameters for the 20% Al α-Ni(OH)$_2$ in the charge–discharge processes. The phase transformation from the α-Ni(OH)$_2$ to the γ-NiOOH was accompanied by the decrease in the *a* and *c* lattice constant because of the decrease in the ionic radius of nickel (Ni^{2+} (0.69 Å), Ni^{3+} (0.56 Å), and Ni^{4+} (0.48 Å)) on the nickel sites [15]. The *c* lattice constant for the fault phases was slightly larger than those for ideal phases. The lattice volume change (21.3%) for the α-Ni(OH)$_2$/γ-NiOOH phase

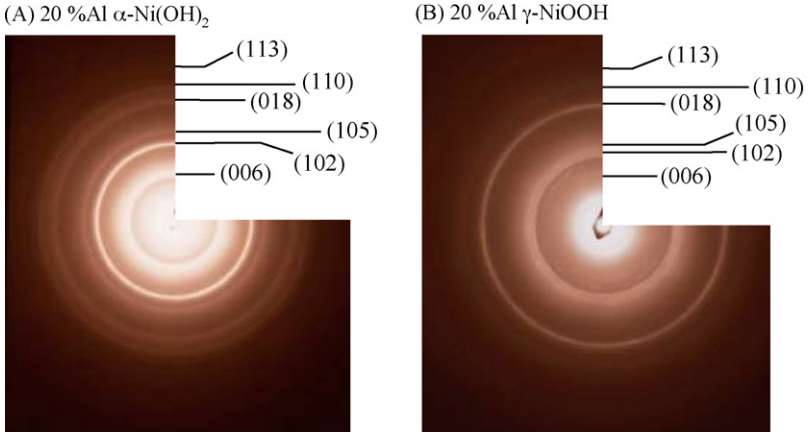

Fig. 8. The ED patterns for (A) the 20% Al α-Ni(OH)$_2$ and (B) the 20% Al γ-NiOOH.

Table 4
The observed *d*-values for the 20% Al α-Ni(OH)$_2$ and γ-NiOOH derived from the XRD patterns and the ED patterns.

20% Al α-Ni(OH)$_2$			20% Al γ-NiOOH		
(*h k l*)	*d*-Values for XRD patterns (nm)	*d*-Values of ED patterns (nm)	(*h k l*)	*d*-Values for XRD patterns (nm)	*d*-Values of ED patterns (nm)
0 0 3	0.777	Being buried in the spot	0 0 3	0.702	Being buried in the spot
0 0 6	0.389	0.387	0 0 6	0.351	0.348
1 0 2	0.257	0.252	1 0 2	0.243	0.248
1 0 5	0.229	0.224	1 0 5	0.209	0.211
0 1 8	0.150	0.148	0 1 8	0.141	0.144
1 1 0	0.141	0.140	1 1 0	0.138	0.139
1 1 3	0.127	0.128	1 1 3	0.130	0.128

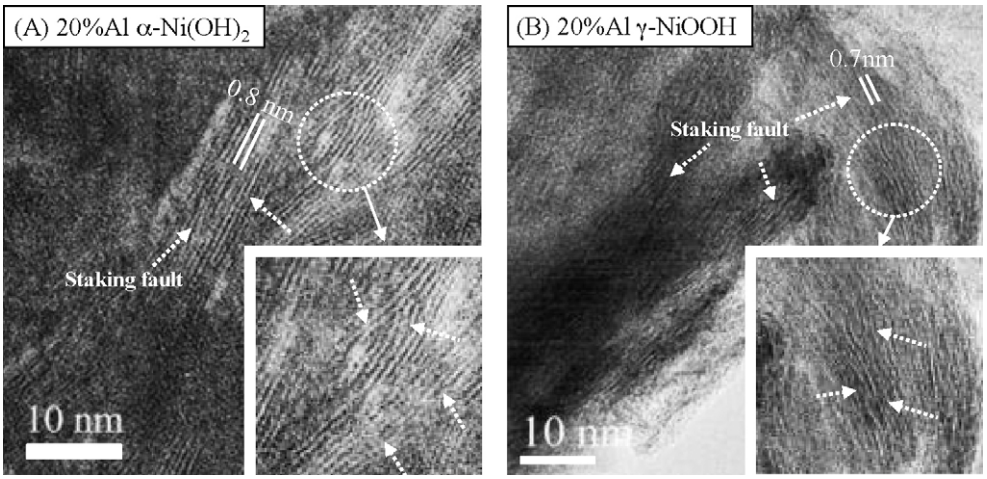

Fig. 9. The high-resolution TEM images for (A) the 20% Al α-Ni(OH)$_2$ and (B) the 20% Al γ-NiOOH.

transformation was much larger than those (14.2%) for the β-Ni(OH)$_2$/β-NiOOH phase transformation.

Fig. 8(A) and (B) shows the electron diffraction (ED) patterns for the 20% Al α-Ni(OH)$_2$ and γ-NiOOH, respectively. The 20% Al α-Ni(OH)$_2$ and γ-NiOOH were transformed to the NiO by the exposure to the electron beam for long time. The stacking faults for the 20% Al α-Ni(OH)$_2$ and γ-NiOOH could be observed for several seconds using the thinner sample prepared by a microtome machine.

Those ED patterns were indexed on the basis of a rhombohedral unit cell. The observed *d*-values for the ED patterns were in agreement with those for the XRD patterns. This result shows that the samples were not damaged by the electron beam. The observed *d*-values for the 20% Al α-Ni(OH)$_2$ and the 20% Al γ-NiOOH derived from the ED patterns and the XRD patterns are summarized in Table 4.

Fig. 9(A) and (B) shows the TEM images for the 20% Al α-Ni(OH)$_2$ and γ-NiOOH, respectively. The samples are the polycrystal consisting of the rod-like grains with the layered structure. The observed values of the layer distance in the grains were estimated to be 0.8 nm for the α-Ni(OH)$_2$ and 0.7 nm for the γ-NiOOH, respectively, in

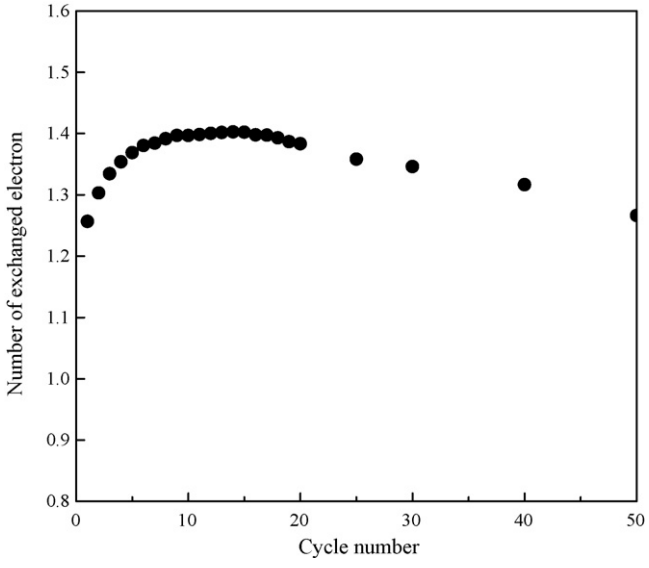

Fig. 10. The cycle performance for the Ni-MH test cell using the 20% Al α-Ni(OH)$_2$.

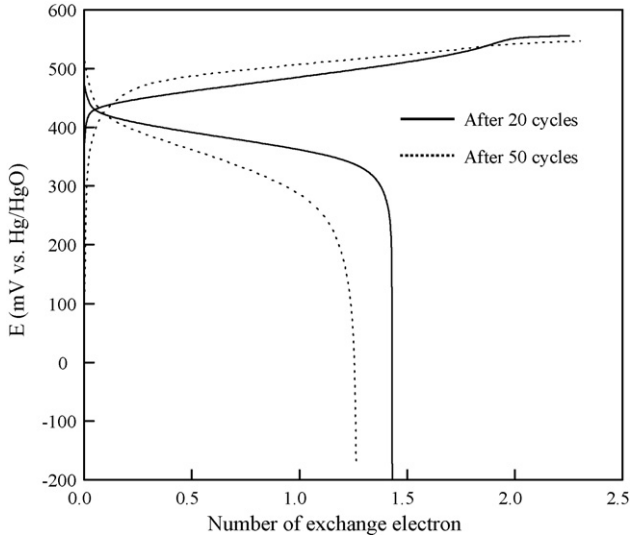

Fig. 11. The charge–discharge curves for the Ni-MH test cells using the 20% Al α-Ni(OH)$_2$ after 50 charge–discharge cycles.

Table 5
Summary of the *R* factors and the crystallographic parameters for the 20% Al $Ni(OH)_2$ obtained at various values of NEE determined by the Rietveld refinements after 50 charge–discharge cycles.

NEE	Phase	R_{wt} (%)	*Re* (%)	*S*	Cell parameters (Å)	Volume (Å^3)	Content (wt%)
0	Ideal β-$Ni(OH)_2$	5.86	3.60	1.6304	*a* = 3.058 (2), *c* = 23.47 (5)	190.1	30.0
	Fault β-$Ni(OH)_2$				*a* = 3.072 (2), *c* = 23.53 (8)	192.5	9.0
	Ideal α-$Ni(OH)_2$				*a* = 3.137 (9), *c* = 4.689 (2)	39.98	41.6
	Fault α-$Ni(OH)_2$				*a* = 3.130 (6), *c* = 4.697 (3)	39.87	8.3
	CoOOH				*a* = 2.856 (8), *c* = 13.34 (9)	93.99	11.1
2.25	Ideal γ-NiOOH	6.79	3.88	1.7492	*a* = 2.822 (5), *c* = 21.23 (1)	146.4	76.6
	Fault γ-NiOOH				*a* = 2.844 (1), *c* = 21.37 (7)	149.7	18.2
	CoOOH				*a* = 2.855 (2), *c* = 13.33 (5)	93.97	5.2

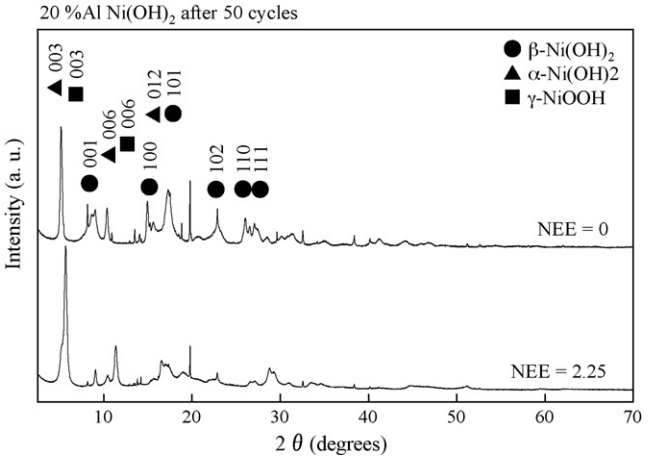

Fig. 12. The XRD patterns for the 20% Al α-$Ni(OH)_2$ obtained at various values of NEE after 50 charge–discharge cycles.

agreement with the *c* lattice constant derived from the XRD patterns for each sample. The enlarged TEM images showed the disordered stacking structure as pointed with arrows in Fig. 9, suggesting the presence of stacking faults for the 20% Al α-$Ni(OH)_2$ and γ-NiOOH. Similar stacking faults have been reported for β-$Ni(OH)_2$ [16].

Fig. 10 shows the cycle performance for the Ni-MH test cells using the 20% Al α-$Ni(OH)_2$. The NEE values reached 1.41 at 20 cycles, and then were decreased up to 1.26 at 50 cycles. The NEE values decrease after 50 cycles because of the phase transformation from the α-$Ni(OH)_2$ to the β-$Ni(OH)_2$.

Fig. 11 shows the charge–discharge curves for the Ni-MH test cells using the 20% Al α-$Ni(OH)_2$ after 20 and 50 charge–discharge cycles. The charge potential was increased and the discharge potential was decreased after 50 cycles, suggesting the increase in the internal resistance.

Fig. 12 shows the XRD patterns for the 20% Al α-$Ni(OH)_2$ at various values of NEE after 50 charge–discharge cycles. At NEE = 0, the XRD patterns are characterized as the mixture phases of an α-$Ni(OH)_2$ and a β-$Ni(OH)_2$. The phase abundance for the α-$Ni(OH)_2$ and the β-$Ni(OH)_2$ was about 49.9 and 39.0%, respectively. The 20% Al α-$Ni(OH)_2$ became unstable in the long charge–discharge process because the aluminum ions on the 18h sites would be migrated from the bulk to the surface. At NEE = 2.25, both the α-$Ni(OH)_2$ and the β-$Ni(OH)_2$ were transformed to the γ-NiOOH. The structural parameters for the 20% Al α-$Ni(OH)_2$ at various values of the NEE derived from the Rietveld refinements after 50 cycles are summarized in Table 5.

4. Conclusion

The detailed structure change in the charge–discharge process has been revealed for a 20% Al α-$Ni(OH)_2$ by using high-resolution synchrotron XRD, XAFS and TEM analysis. The 20% Al α-$Ni(OH)_2$ showed the α-$Ni(OH)_2$/γ-NiOOH phase transformation in the charge–discharge process. The structural refinement for the 20% Al α-$Ni(OH)_2$ has been done successfully on the basis of two phase models of the ideal phases and the fault ones. The fault phases contained a larger amount of intercalated potassium ions and H_2O (OH^-) molecules than the ideal ones. The aluminum ions occupied both nickel sites and 18h sites in the interlayer. The 20% Al α-$Ni(OH)_2$ became unstable in the long charge–discharge process because the aluminum ions on the 18h sites would be migrated from the bulk to the surface.

Acknowledgment

The XAFS measurement was financially supported by SPring-8 Industrial Application Proposals. The authors are grateful to Dr. M. Sugiura, Dr. T. Honma, Dr. M. Sato, Mr. T. Matsumoto, and Ms. S. Hirayama at Japan Synchrotron Radiation Research Institute (JASRI) for the synchrotron XRD and XAFS measurements, and those analyses.

The authors are grateful to Professor Y. Kitano at Hiroshima Institute of Technology for the TEM observations, and those analyses.

References

[1] M. Kodama, M. Kanemoto, S. Ochiai, M. Miyamoto, M. Kuzuhara, M. Watada, M. Oshitani, YUASA-JIHO 95 (2003) 7–11.
[2] T. Ozaki, M. Kanemoto, T. Kakeya, Y. Kitano, M. Kuzuhara, M. Watada, S. Tanase, T. Sakai, J. Alloys Compd. 446–447 (2007) 620–624.
[3] R. Barnard, C.F. Randell, F.L. Tye, J. Appl. Electrochem. 10 (1980) 109–125.
[4] P.V. Kamath, M. Dixit, L. Indira, A.K. Shukla, V.G. Kumar, N. Munichandraiah, J. Electrochem. Soc. 141 (1994) 2956–2959.
[5] M. Dixit, R.S. Jayashree, P.V. Kamath, A.K. Shukla, V.G. Kumar, N. Munichandraiahc, Electrochem. Solid State Lett. 2 (1999) 170–171.
[6] A. Sugimoto, S. Ishida, K. Hanawa, J. Electrochem. Soc. 146 (1999) 1251–1255.
[7] R.S. Jayashree, P.V. Kamath, J. Appl. Electrochem. 31 (2001) 1315–1320.
[8] H. Chen, J.M. Wang, T. Pan, Y.L. Zhan, J.Q. Zhang, C.N. Cao, J. Power Sources 143 (2005) 243–255.
[9] C. Delmas, C. Tessier, J. Mater. Chem. 7 (1997) 1439–1443.
[10] C. Tessier, P.H. Haumesser, P. Bernard, C. Delmas, J. Electrochem. Soc. 146 (1999) 2059–2067.
[11] F. Izumi, T. Ikeda, Mater. Sci. Forum 321–324 (2000) 198–203.
[12] T. Taguchi, T. Ozawa, H. Yashiro, Phys. Scripta T 115 (2005) 205–206.
[13] O. Glemser, J. Einerhand, Z. Anorg. Allg. Chem. 261 (1950) 43–51.
[14] R.S. McEwen, J. Phys. Chem. 75 (1971) 1782–1789.
[15] R.D. Shannon, Acta Crystallogr., Sect. A 32 (1976) 751–767.
[16] M. Casas-Cabanas, J. Rodriguez-Carvajal, J. Canales-Vaĭzqueza, M. Rosa Palacin, J. Mater. Chem. 16 (2006) 2925–2939.